Determinants of target prioritization and regulatory hierarchy for the bacterial small RNA SgrS

Maksym Bobrovskyy[1,2] Jane K. Frandsen[3,4], Jichuan Zhang[5], Anustup Poddar[5], Muhammad S. Azam[1], Tina M. Henkin[3], Taekjip Ha[5,6] and Carin K. Vanderpool[1]*

[1]Department of Microbiology, University of Illinois at Urbana-Champaign, 601 S. Goodwin Ave., Urbana, Illinois 61801
[2]Present address: Department of Microbiology, The University of Chicago, 920 E. 58th St., Chicago, Illinois 60637
[3]Department of Microbiology and Center for RNA Biology, The Ohio State University, Columbus, Ohio 43210
[4]Biochemistry Program, The Ohio State University
[5]Department of Biophysics and Biophysical Chemistry, Johns Hopkins University, Baltimore, Maryland, USA 21205
[6]Howard Hughes Medical Institute, Baltimore, Maryland, USA 21205

*Corresponding author
Carin K. Vanderpool, Ph.D.
Department of Microbiology
University of Illinois at Urbana-Champaign
C213 CLSL, MC-110
601 S. Goodwin Ave.
Urbana, IL 61801
(t) 217-333-7033
(f) 217-244-6697
cvanderp@life.illinois.edu

Running title: Target prioritization by small RNAs

Abstract word count: 241

Text word count: 6,690

ABSTRACT

The mechanisms by which small RNA (sRNA) regulators select and prioritize target mRNAs remain poorly understood, but serve to promote efficient responses to environmental cues and stresses. We sought to uncover mechanisms that establish regulatory hierarchy for a model sRNA, SgrS, found in enteric bacteria and produced under conditions of metabolic stress when sugar transport and metabolism are unbalanced. SgrS post-transcriptionally controls a nine-gene regulon to restore growth and homeostasis under stress conditions. An *in vivo* reporter system was used to quantify SgrS-dependent regulation of target genes and established that SgrS exhibits a clear preference for certain targets, and regulates those targets efficiently even at low SgrS levels. Higher SgrS concentrations are required to regulate other targets. The position of targets in the regulatory hierarchy is not well-correlated with the predicted thermodynamic stability of SgrS-mRNA interactions or the SgrS-mRNA binding affinity as measured *in vitro*. Detailed analyses of SgrS interaction with *asd* mRNA demonstrate that SgrS binds cooperatively to two sites and remodels *asd* mRNA secondary structure. SgrS binding at both sites increases the efficiency of *asd* mRNA regulation compared to mutants that have only a single SgrS binding site. Our results suggest that sRNA selection of target mRNAs and regulatory hierarchy are influenced by several molecular features. The sRNA-mRNA interaction, including the number and position of sRNA binding sites on the mRNA and cofactors like the RNA chaperone Hfq, seem to tune the efficiency of regulation of specific mRNA targets.

IMPORTANCE

To survive, bacteria must respond rapidly to stress and simultaneously maintain metabolic homeostasis. The small RNA (sRNA) SgrS mediates the response to stress that arises from imbalanced sugar transport and metabolism. To coordinate the stress response, SgrS regulates genes involved in sugar uptake and metabolism. Intrinsic properties of sRNAs such as SgrS allow them to regulate extensive networks of genes. To date, sRNA regulation of targets has largely been studied in the context of “one sRNA-one target”, and little is known about coordination of multi-gene regulons and sRNA regulatory network structure. Here, we explore the molecular basis for regulatory hierarchy in sRNA regulons. Our results reveal a complex interplay of factors, including the number and location of sRNA binding sites on mRNA targets and the participation of an RNA chaperone, that dictate prioritized regulation of targets to promote an efficient response to stress.

INTRODUCTION

Bacteria live in diverse niches, often encountering rapidly changing and stressful environments. Bacterial stress responses can mitigate the negative effects of stress on cell structure and function. Stress responses are usually coordinated by molecules, either RNAs or proteins, that alter expression of a regulon comprised of multiple genes. Coordinated control of the regulon prepares the cell to survive or adapt to the stress (1). Proteins control expression of target regulons by binding to DNA sequences and modulating the frequency of transcription initiation, whereas RNAs often modulate gene expression post-transcriptionally. A prevalent type of RNA regulator in bacteria is referred to simply as small RNA (sRNA). The sRNAs are often produced in response to a particular stress, and regulate target mRNAs through base pairing interactions that modify mRNA translation or stability (2, 3). Hundreds of sRNAs have been identified in diverse bacteria (4-6). While the majority of sRNAs have not been characterized, many studies suggest that sRNA regulatory networks are as extensive and complex as those controlled by proteins (7, 8).

A large body of work has illuminated base pairing-dependent molecular mechanisms of post-transcriptional regulation by sRNAs (9, 10). The sRNA SgrS (sugar-phosphate stress sRNA) has been an important model for discovery of both negative and positive mechanisms of target mRNA regulation. SgrS is induced in response to metabolic stress associated with disruption of glycolytic flux and intracellular accumulation of sugar phosphates (also referred to as glucose-phosphate stress) (11, 12). SgrS regulates at least 9 genes and promotes recovery from glucose-phosphate stress. SgrS-dependent repression of mRNAs encoding sugar transporters

(*ptsG, manXYZ*) reduces uptake of sugars to prevent further sugar-phosphate accumulation (Fig. 1) (11, 13, 14). Activation of a sugar phosphatase (*yigL*) mRNA promotes dephosphorylation and efflux of accumulated sugars (15), and repression of other mRNAs is hypothesized to reroute metabolism to promote recovery from stress (Fig. 1) (16). Each target of SgrS is regulated by a distinct molecular mechanism. How different mechanisms of regulation yield effects of variable magnitude with respect to mRNA stability and translation is an open question.

Temporally-ordered and hierarchical patterns of gene regulation carried out by protein transcription factors have been characterized in many systems (17-20). These regulatory patterns allow cells to respond efficiently to environmental signals by prioritizing induction or repression of products needed to respond to those signals. Protein regulators establish a hierarchy of regulation based on their affinities for binding sites in the operator regions of different target genes. As the concentration of active regulator increases, genes are sequentially regulated based on binding site affinity (21). There is growing evidence that sRNAs also regulate their target genes hierarchically (22, 23). However, the mechanisms involved in establishing and maintaining prioritized regulation of sRNA targets are not known.

We hypothesize that the temporal progression of target regulation by SgrS is optimized to promote efficient recovery from glucose-phosphate stress (Fig. 1). To test this hypothesis, we first defined the efficiency of SgrS regulation of each target and found that SgrS indeed prioritizes regulation of some targets over others. We examined the factors that determine regulatory efficiency, including the arrangement and strength of SgrS target binding sites and the roles of other factors like RNase E and Hfq.

Detailed characterization of a specific SgrS-mRNA target interaction revealed cooperative binding of SgrS to two binding sites and a requirement for both binding sites for maximal SgrS-dependent regulation. Collectively, our results uphold the hypothesis that sRNAs regulate expression of genes in their target regulons hierarchically, and that this is influenced by features of each sRNA-mRNA pair and different molecular mechanisms of regulation that precisely determine the regulatory priority for each target.

RESULTS

SgrS differentially regulates targets at the level of translation. Previous studies suggested the possibility of a regulatory hierarchy for the small RNA SgrS, which regulates a diverse set of mRNA targets (10, 11, 13-15). To study this, we used a two-plasmid system to control expression of SgrS and target translational fusions (Fig. 2A). All target transcript fragments fused to *gfp* contain experimentally-confirmed SgrS binding sites. To quantify translational regulation by SgrS and facilitate comparisons of regulatory efficiency among targets, we analyzed the data as described previously (23). Activity of reporter fusions was measured by monitoring GFP fluorescence over time. By plotting the GFP fluorescence (RFU) as a function of growth (OD_{600}) for target-*gfp* fusions in the absence of SgrS, we defined “basal activity” at different inducer concentrations (example in Fig. S1A). This method of quantifying fusion activity accounts for the fact that fluorescence levels are not directly proportional to inducer concentrations ((23) and Fig. S1A). While the absolute values for basal activity differ among different fusions, all fusions responded to induction in a dose-dependent manner (Fig. S2A). Similar plots (RFU/OD_{600}) were generated for each fusion in the presence of SgrS (examples Fig. S1B-F). We define “regulated activity” as the slope of the curve

(RFU/OD_{600}) under conditions where both the fusion and SgrS are induced (example in Fig. S1B). As levels of SgrS increase, clear patterns of repression or induction are seen for all target fusions (Figs S1B-F and S2B-F).

To define the efficiency of regulation of each target, we plotted regulated activity as a function of basal activity for *ptsG*, *manX, asdI, purR,* and *yigL*. When there is no SgrS-mediated regulation, a line with a slope of 1 is seen for all targets (Fig. 2B-F). Slopes less than 1 indicate that the fusion is repressed by SgrS. This is true for *ptsG*, *manX*, *asdI* and *purR* reporter fusions (Figure 2B-E). Slopes greater than 1 are indicative of activation by SgrS, as seen for *yigL* (Fig. 2F). The magnitude of regulation was responsive to SgrS levels over the range of SgrS inducer (aTc) concentrations (Fig. 2B-E). In contrast, for for *yigL,* the magnitude of activation did not increase beyond a maximal level obtained at 20 ng/mL of inducer (Fig. 2F). While the basis for this difference is unclear, it is likely to reflect the inherently different molecular mechanisms of regulation, *i.e.,* mRNA stabilization for *yigL* and translational repression for other targets.

We then compared regulatory efficiency of targets at different levels of SgrS induction. At the two lowest levels of SgrS induction (10ng/mL and 20 ng/mL aTc), only *ptsG* and *yigL* showed substantial repression and activation, respectively (Fig. 3A, B). In contrast, *manX*, *asdI* and *purR* fusions yielded curves whose slopes remained at ~1, indicating no regulation at lower levels of SgrS. Our interpretation is that *ptsG* and *yigL* are high-priority targets of SgrS, since they are regulated preferentially when SgrS levels are low. With increasing SgrS levels (20-50 ng/ml aTc), regulation of “weaker” targets *manX, asdI* and *purR* became apparent (Fig. 3C, D, E). As SgrS levels

increased, *ptsG* repression became more efficient up to a maximal repression at 40 ng/mL of aTc, and it remained the most strongly repressed target at all levels of SgrS. Collectively, these data suggest that SgrS targets are preferentially regulated in the following order: 1/2) *ptsG* and *yigL*, 3) *manX,* 4) *asdI*, and 5) *purR* (Fig. 3A-E). We hypothesize that the position of each target within the regulatory hierarchy is determined by characteristics of SgrS-target mRNA interactions and the mechanism of SgrS-dependent regulation.

Differences in binding affinity *in vitro* are not correlated with regulation efficiency. One of the initial steps in sRNA-mediated regulation is formation of base-pairing interactions with the target mRNA. Binding of the sRNA with its target mRNA is dependent on sequence complementarity and RNA secondary structure. We examined the characteristics of SgrS-target mRNA binding *in vitro* to determine whether the strength of binding is correlated with the target hierarchy.

Electrophoretic mobility shift assays (EMSAs) were performed to measure binding of SgrS to its target mRNAs *ptsG*, *manX*, *purR*, *yigL* and *asd*. SgrS bound to *ptsG* with a K_D of 0.11 ± 0.01 μM (Fig. 4A, B), which was lower than K_Ds for SgrS binding to most of the other targets (Fig. 4A-E). SgrS-*manX* mRNA binding had a K_D of 19.7 ± 2.78 μM (Fig. 4A, C), which is weaker than the interaction with *ptsG* (Fig. 4B), but stronger compared to *purR* and *yigL* (Fig. 4A). Three different fragments of *asd* mRNA were tested, because previous work demonstrated that SgrS pairs at two distinct sites on *asd* mRNA (16). The first site, *asdI*, is adjacent to the ribosome binding site and is sufficient for modest SgrS-dependent translational repression. The second site, *asdII,* is in the coding sequence of *asd,* 60-nt downstream of the start codon. When both sites

are present (RNA *asdI-II*), stronger SgrS-dependent translational repression was observed (16). Surprisingly, while *asdI* RNA (containing only the upstream SgrS binding site) regulation was less efficient compared to that of *manX* (Fig. 3A-E), *in vitro* it bound SgrS more strongly with a K_D of 0.15 ± 0.04 μM (Fig. 4A, D), which is comparable to SgrS-*ptsG* binding (Fig. 4A, B). SgrS interaction with *asdII* was very weak (Fig. 4A). We could not determine K_D values for SgrS interaction with *asdII*, *purR* and *yigL*, due to limitations in obtaining high enough concentrations of RNA, but it is apparent that SgrS binding to these targets is much weaker compared to *ptsG*, *manX* and *asdI* (Fig. 4A).

Results of EMSAs with SgrS and *asdI-II* (containing both SgrS binding sites) revealed apparent binding cooperativity. SgrS binding to *asdI-II* has a K_D of 0.07 ± 0.01 μM (Fig. 4E, F), slightly lower than that of SgrS-*ptsG* mRNA binding. Moreover, we observed two shifted species that correspond to binding of either one or two SgrS sRNAs to a single *asdI-II* RNA (Fig. 4E).

Structural analyses of SgrS-*asd* mRNA interactions. Our data thus far indicate that SgrS regulates mRNA targets in a hierarchical fashion (Figs. 2, 3). However, SgrS-mRNA binding affinities do not explain the target hierarchy, as SgrS-*ptsG* mRNA and SgrS-*asd* mRNA interactions have very similar K_Ds, but *ptsG* is much more efficiently regulated than *asd* at all concentrations of SgrS (Fig. 3). To further understand the features that influence the efficiency of target regulation, we performed more detailed analyses of SgrS-*asd* mRNA interactions.

Previous work demonstrated that SgrS binding site I encompasses nt +31 to +49 and site II encompasses nt +110 to +127 ((16), Fig. 5A). We used IntaRNA (24, 25) to predict the free energy (ΔG) for SgrS interactions with *asd* mRNA segments containing

both sites, or each site individually (Fig. 5B). IntaRNA accounts for the energy of opening double-stranded RNA secondary structure, to make sequences accessible for pairing. We first analyzed SgrS interactions with *asdI-II* mRNA (nt +1 to +240), which we denote as "structured." Interaction of SgrS with *asd* site I has a predicted ΔG of -10.5 kcal/mol, while SgrS pairing with site II has a predicted ΔG of -1.1 kcal/mol (Fig. 5B, structured). The ΔG for interactions between SgrS and the isolated binding sites are -18 kcal/mol for site I and -7.4 kcal/mol for site II (Fig. 5B, isolated). These predictions suggest that SgrS interaction with site II is less favorable, particularly in the context of the longer structured *asd* mRNA.

We investigated the structure of *asdI-II* with selective 2'-hydroxyl acylation analyzed by primer extension (SHAPE), in which flexible nts are modified by N-methylisotoic anhydride (NMIA), while nts constrained in helices are not reactive. In the absence of SgrS, the sequence encompassing the *asd* ribosome binding site (+44 to +50) is located within a structured loop (+36 to +69) on top of a short stem (+31 to +35 pairing with +70 to +74) (Fig. 5C, Fig. S3). The nts in site I (+31 to +49, Fig. 5A) are located on the 5' side of the stem-loop structure. Most of the nts in this structure are reactive, which is indicative of a flexible conformation that is accessible for ribosome binding or base pairing with the seed sequence of SgrS (Fig. 5C). The seed interaction of SgrS is likely to promote opening of the structure. Downstream of the site I stem-loop structure is a highly structured second stem (+83 to +155) that contains site II in the apical region (+110 to +129) (Fig. 5C, Fig. S3). Site II is sequestered in a helix and would not be accessible to base pair with SgrS (Fig. 5C). In light of binding cooperativity

observed in Fig. 4E, we hypothesize that SgrS pairing with site I induces rearrangement of *asd* mRNA secondary structure to facilitate interaction with site II.

We next used SHAPE to probe changes in the *asdI-II* structure in the presence of SgrS. The reactivity of site I nt +31 to +49 decreased as the concentration of SgrS increased (Fig. 5D), with the exception of nt +41 which is not predicted to base pair with SgrS (Fig. 5A). The SHAPE reactivity plateaued between 5- and 10-fold excess SgrS (Fig. S3E,F), which suggests that binding to site I was saturated. This is consistent with a strong base-paring interaction between SgrS and site I. In contrast, the reactivity of the site II nts +110 to +129 decreased more slowly and to a lesser extent (Fig. 5D), consistent with a weaker and cooperative interaction. Fewer site II nts showed changes in SHAPE reactivity upon addition of SgrS; this is likely to be due to the highly structured nature of site II in the absence of SgrS.

The reactivity of nts outside of the SgrS binding sites also changed in the presence of SgrS (Fig. 5E). In contrast, when a mutant SgrS that is not predicted to bind to *asdI-II* was used, minimal changes in SHAPE reactivity were observed, which suggests that the changes in the presence of wild-type SgrS are due to the specific interactions between SgrS and *asdI-II* mRNA and not to the presence of additional RNA in the system (Fig. 5E). These results indicate that SgrS binding changes the overall structure of the *asd* RNA. A secondary structure predicted using the SHAPE data suggests that these changes are limited to opening the SgrS binding sites and extending the site II stem (Fig. 5C). We note an important caveat to these analyses. The structure prediction algorithms were not designed to account for intermolecular interactions, so this analysis may not be able to capture the *in vivo* relevant structure of

asd mRNA in complex with SgrS. Nonetheless, SHAPE data are consistent with other analyses in demonstrating binding of SgrS to *asd* mRNA, prominently at site I and to a lesser extent at site II.

Optimal repression by SgrS involves both pairing sites within *asd* mRNA. To further investigate the role of the two SgrS pairing sites on *asd*, we performed stochastic optical reconstruction microscopy (STORM) coupled with single-molecule *in situ* hybridization (smFISH) to monitor SgrS regulation of *asd-lacZ* variants *asdI, asdII,* and *asdI-II* (Fig. 6A) at single molecule resolution. In these experiments, bacteria were grown in the presence of L-arabinose to induce expression of chromosomal *asd-lacZ* variants, and glucose-phosphate stress was induced for 10 min by the addition of 1% α-methyl D-glucopyranoside (αMG). 3D super-resolution images show *asd-lacZ* mRNAs (Fig. 6B-D, green) and SgrS (Fig. 6B-D, red), as projected on 2D planes, with cells outlined. Numbers of *asd-lacZ* mRNAs and SgrS sRNAs were counted and represented as “copy number per cell” in histograms, with average copy number per cell indicated above the histogram (Fig. 6B-D). SgrS induction reduced the copy number of *asdI-lacZ* RNA by 3-fold (Fig. 6B, green) when SgrS was induced to high levels after 10 min treatment with αMG (Fig. 6B, red and S4A, B). In contrast, the copy number of *asdII-lacZ* RNAs (Fig. 6C, green) was not strongly affected in the presence of high SgrS levels after αMG treatment (Fig. 6C, red and Fig. S4C, D). Copy numbers of *asdI-II-lacZ* RNA (Fig. 6D, green) were reduced by ~8-fold after 10 min of αMG induction (Fig. 6D, red, Fig. S6E,F). These data demonstrate that both binding sites on *asd* mRNA are important for efficient SgrS-dependent regulation of mRNA stability.

We next examined the roles of the two SgrS binding sites in the efficiency of translational regulation. SgrS regulation of an *asdI-II* translational fusion was compared to regulation of an *asdI* fusion (Fig. 7A). By plotting regulated activity as a function of basal activity as described above, we determined that SgrS repression of *asdI-II* was more efficient than repression of *asdI* across a range of SgrS expression levels (Fig. 7B), a result in line with our previous study (16). Comparison to other targets indicated that *asdI-II* is regulated more efficiently than *manX*, *asdI* and *purR*, at all concentrations of SgrS (Fig. 7C).

We then compared SgrS regulation of *asdI* and *asdI-II* in the *rne701* mutant strain deficient in degradosome assembly (26). We determined basal activity (Fig. S5A) and regulated activity (Fig. S5B-F) of *asdI* and *asdI-II* translational *gfp* fusions at different levels of SgrS induction. Similar to our data for the wild-type strain (Fig. 7A), SgrS regulated *asdI-II* more efficiently compared to *asdI* in the *rne701* mutant (Fig. 7D). Moreover, when compared to SgrS regulation of other targets, *asdI-II* was repressed most efficiently (Fig. 7E) in the *rne701* mutant. Taken together the data indicate that the second binding site on *asd* mRNA enhances the stringency of SgrS-mediated regulation. Moreover, addition of the second binding site on *asd* changes its regulatory priority relative to other targets in the SgrS regulon.

Transcriptional regulation of *asd* by SgrS. We observed that the *asdI-II* RNA is more abundant than *asdI* (Fig. 6B, D). Since the constructs used in that experiment were expressed from a heterologous promoter, we postulated that increased levels of *asdI-II* compared to *asdI* mRNA must be due to increased mRNA stability or transcription elongation of the *asdI-II* construct compared to *asdI.* We therefore constructed *asdI* and

asdI-II transcriptional fusions to *lacZ* expressed from an inducible promoter (Fig. 8A) to test whether SgrS can regulate *asd* transcripts independent of translational regulation. Consistent with observations from smFISH, the *asdI-II-lacZ* transcriptional fusion had substantially higher activity compared to *asdI-lacZ* (Fig. 8B). Repression of *asdI-II* by SgrS was more efficient (3.3-fold repression) than was observed for *asdI* (2.1-fold repression) (Fig. 8B). SgrS still regulated both fusions in the *rne701* mutant strain (Fig. 8B). Importantly, SgrS-dependent degradation of other SgrS targets (*ptsG* mRNA (27) and *manXYZ* mRNA (13, 14)) was abolished in degradosome mutants. Together with our previous work, these observations suggest that SgrS regulates *asd* by two independent mechanisms, translational repression by pairing at site I (directly occluding the ribosome binding site) and reducing mRNA levels by promoting mRNA turnover and/or inhibiting transcription elongation.

DISCUSSION

In this study, we set out to define the hierarchy of regulation by a model bacterial sRNA. SgrS is a good model for this study because it has a modestly-sized regulon, and the mechanisms of regulation of several targets have been characterized in detail (13, 15, 16, 28). Our results demonstrate a clear pattern of prioritized regulation of mRNA targets (Fig. 2B-F, Fig. 3A-E). Two targets in particular, *ptsG* and *yigL,* were “high-priority” targets that were efficiently regulated even at low levels of SgrS. Other targets, *manX, purR,* and *asd,* were less impacted by SgrS and were regulated only when SgrS was produced at higher levels.

We investigated features of sRNA-mRNA interactions that could impact the overall efficiency of SgrS-mediated regulation. SgrS-mRNA interactions *in vitro*, as

measured by EMSA defined K_Ds, were not well-correlated with *in vivo* regulatory efficiency (Fig. 4A-F, Fig. 3A-E). Two targets stood out in the comparison of *in vivo* regulation and *in vitro* SgrS-mRNA interactions. The *yigL* mRNA interaction with SgrS was barely detectable *in vitro* (Fig. 4A), but *in vivo*, *yigL* translation was maximally activated at low SgrS levels (Fig. 2F). Conversely, the translation of *asdI* was modestly regulated by SgrS *in vivo* (Fig. 2E), but the *in vitro* SgrS-*asdI* interaction was comparable to that of SgrS-*ptsG*, which had the strongest *in vivo* regulatory effect. These apparent contradictions between *in vitro* interactions and *in vivo* regulatory efficiency led us to further explore SgrS regulation of *asd.*

Previous work demonstrated that SgrS has two binding sites on *asd* mRNA: site I overlaps that *asd* ribosome binding site and site II is ~60 nt downstream in the *asd* coding sequence ((16) and Fig. 5A). EMSAs demonstrated SgrS pairing at site I alone, but pairing at site II alone was undetectable. Binding of SgrS to an *asd* mRNA containing both sites I and II was cooperative (Fig. 4E,F). Structural analyses of *asd* mRNA in the absence and presence of SgrS demonstrated that SgrS indeed pairs preferentially at site I over site II and induces substantial structural rearrangement in the mRNA (Fig. 5C-E, Fig. S3). Quantification of SgrS-dependent degradation of *asd* mRNA showed that site I is important, but sites I and II together promote the most efficient regulation (Fig. 6B-D, Fig. S4). Similar to binding and regulation of mRNA degradation, SgrS interactions at both sites I and II on *asd* mRNA improve the efficiency of translational regulation (Fig. 7B,C, Fig. S2). These results suggest that the number and position of sRNA binding sites on mRNA targets control regulation *in vivo* in ways that could not be predicted based on *in vitro* characterization of sRNA-mRNA binding.

346 In many cases, sRNA-mediated regulation of translation is thought to indirectly
347 affect mRNA stability by making untranslated mRNA more susceptible to degradation by
348 RNase E. There are also examples of sRNA regulation, including SgrS regulation of
349 *yigL* (15), where modulation of mRNA stability is translation-independent. Truncation of
350 RNase E (encoded by *rne*), removing the C-terminal scaffold for degradosome
351 assembly, often prevents sRNA-mediated degradation of mRNA targets (14, 29, 30). If
352 translational regulation is the primary function of an sRNA on a given mRNA target, the
353 regulation should be preserved in *rne* mutant backgrounds. For SgrS targets, the
354 regulatory hierarchy is mostly preserved in an *rne701* degradosome mutant background
355 (Fig. 7, compare C and E), suggesting that for most targets, regulation of RNA stability
356 is not the primary mechanism of control by SgrS. Interestingly, the high-priority target
357 *ptsG* was a notable exception. In the wild-type background, *ptsG* is the most efficiently-
358 regulated target (Fig. 7C), whereas in the *rne701* host, it is weakly regulated. This
359 defect could be overcome by increasing SgrS expression levels (Fig. S6B). This result
360 suggests that RNase E-dependent degradation of *ptsG* mRNA is more important for its
361 efficient regulation by SgrS compared to other targets, where efficient regulation does
362 not depend on subsequent target degradation. This is consistent with the fact that *ptsG*
363 mRNA levels decrease at least 10-fold whereas other targets exhibit a modest 2-fold
364 decrease in mRNA levels upon SgrS expression (16). Our recent study quantifying
365 SgrS-dependent mRNA degradation at single molecule resolution indicated that *ptsG*
366 mRNA exhibits faster degradation kinetics than *manXYZ* mRNA (29), which could
367 enhance the efficiency of regulation in a wild-type but not *rne701* mutant background
368 where translational regulation and mRNA degradation are uncoupled.

One of our ultimate goals is to define at a molecular level the mechanisms by which sRNAs select and prioritize regulation of their targets. The current study implicates features of sRNA-mRNA interactions such as number and strength of sRNA binding sites on each mRNA target and accessory factors such as RNase E in dictating regulatory hierarchy. Another factor that is likely to play an important role in setting regulatory priority is the RNA chaperone Hfq. EMSAs demonstrated Hfq binding to *ptsG*, *manX*, *purR*, *yigL*, *asdI*, *asdII* and *asdI-II* mRNAs (Fig. S7A) with similar K_D values for all targets (Fig. S7B). Previous work has shown that sRNAs compete for binding to Hfq, and this competition affects their regulatory ability (31, 32). Different sRNAs can bind to distinct sites on Hfq and this impacts their regulation of particular targets (32, 33). Additional work will be required to determine what role Hfq plays in establishing the hierarchy of regulatory effects in sRNA regulons.

Most sRNA-mRNA interactions are conceived of as single binding site interactions, but we have already identified two SgrS targets that deviate from this model and have shown that additional binding sites can play important roles in regulation and change regulation efficiency (13, 16). We have not yet discovered the specific mechanism of regulation of *asd* mRNA by SgrS, but have shown definitively that both binding sites are required for strong regulation. SgrS-dependent control of both transcriptional and translational *asd* reporter fusions is not impacted in RNase E degradosome deficient strains (Fig. 7B,D, Fig. 8B), suggesting that the regulation is not strictly dependent on translation or mRNA turnover. Future work will test the hypothesis that SgrS acts on *asd* mRNA at the level of transcription elongation, perhaps by an attenuation mechanism.

In *Vibrio*, quorum sensing-regulated Qrr sRNAs regulate multiple targets by distinct mechanisms and differences in those mechanisms influence the dynamics and strength of regulation (22). Strong and rapid regulation is achieved by sRNAs acting catalytically, whereby the sRNA pairs with and promotes mRNA degradation but is then recycled for use on another mRNA target. A sequestration mechanism, where formation of the sRNA-mRNA complex is the terminal outcome of regulation, results in slower and weaker sRNA-dependent regulation of the target mRNA. For Qrr sRNAs, these regulatory mechanisms seem to depend on which region of the sRNA is pairing with a given target and whether the sRNA-mRNA interaction is strong or weak (22). While some of the same features of SgrS-mRNA interactions may be relevant in determining regulatory efficiency, we note that the SgrS seed sequence responsible for pairing with all mRNA targets characterized thus far is encompassed by a short (~20 nt) mostly single-stranded region of SgrS (11, 14-16). Moreover, we did not see a good correlation between strong versus weak binding *in vitro* and *in vivo* regulatory efficiency. It is possible that the “rules” governing regulatory efficiency and specific outcomes are different for each individual sRNA. Detailed analysis of more model sRNAs will be needed to illuminate broad general principles.

Beyond defining interesting molecular features of sRNA-mRNA interactions, defining regulatory hierarchy for sRNA regulons is important for understanding bacterial physiology. The vast majority of sRNA regulons remain undefined, and thus many sRNA functions are unknown. For novel sRNAs, distinguishing high-priority from weaker targets may provide crucial clues to the predominant role of the sRNA in cell physiology. For SgrS, the regulatory hierarchy we have defined here is perfectly consistent with

415 growth studies that demonstrate the primary importance of SgrS regulation of sugar
416 transport and efflux under glucose-phosphate stress conditions (34). The hierarchy of
417 regulation by sRNAs is likely to have evolved to promote rapid and efficient responses
418 to environmental signals that would provide cells with a competitive growth advantage in
419 their specific niche. It will be crucial to develop tools to more rapidly characterize sRNA
420 regulatory hierarchy to better understand the functions of the hundreds of
421 uncharacterized sRNAs in diverse bacteria.

422 **MATERIALS AND METHODS**

423 **Strain and plasmid construction.** Strains and plasmids used in this study are listed in
424 Table S1. All strains used in this study are derivatives of *E. coli* K-12 strain MG1655.
425 Oligonucleotide primers and 5' biotinylated probes used in this study are listed in Table
426 S2 and were purchased from Integrated DNA Technologies. Chromosomal alleles were
427 moved between strains by P1 *vir* transduction (35) and inserted using λ Red
428 recombination (36, 37).

429 Translational reporter fusion alleles P_{BAD}-*asdI-II-lacZ* (MBP151F/MBP193R
430 primers), P_{BAD}-*asdI-lacZ* (MBP151F/MBP151R primers) and P_{BAD}-*asdII-lacZ*
431 (MBP193F/MBP193R primers) were constructed by PCR amplification of desired
432 fragments using primers containing homologies to P_{BAD} and *lacZ.* Similarly,
433 transcriptional fusions P_{BAD}-*asdI-II-lacZ* (MBP151F/MBP206R3 primers) and P_{BAD}-*asdI-*
434 *lacZ* (MBP151F/MBP206R1 primers) were generated by PCR amplification using a
435 forward primer with homology to P_{BAD} and reverse primers containing *lacZ* RBS and
436 *lacZ* homology. PCR products were then recombined into PM1205 strain using λ Red
437 homologous recombination.

438 A plasmid harboring SgrS under the control of P_{tet0-1} promoter was constructed
439 by PCR amplification of *sgrS* from *E. coli* MG1655 chromosomal DNA using primers
440 containing NdeI and BamHI restriction sites. The resulting PCR product and vector
441 pZA31R (23) were digested with NdeI and BamHI (New England Biolabs) restriction
442 endonucleases. Digestion products were ligated using DNA Ligase (New England
443 Biolabs) to produce plasmid pZAMB1 containing P_{tet0-1}-*sgrS* allele.
444 Plasmid pZEMB8 containing P_{lac0-1}-*ptsG-gfp* was constructed by PCR
445 amplification of *ptsG* from MG1655 chromosomal DNA using primers containing KpnI
446 and EcoRI restriction sites. The resulting PCR products and vector pZE12S (23) were
447 digested with KpnI and EcoRI restriction endonucleases. Digestion products were
448 ligated using DNA Ligase to produce pZEMB2. Superfolder *gfp* (referred to as *gfp*) was
449 amplified from pXG10-SF (38) using primrs containing KpnI and XbaI restriction sites.
450 pZEMB2 and the resulting PCR product were digested with KpnI and XbaI, and ligated
451 with DNA ligase to produce pZEMB8. Plasmids with translational reporter fusions P_{lac0-1}-
452 *manX-gfp* (pZEMB10), P_{lac0-1}-*yigL-gfp* (pZEMB15), P_{lac0-1}-*purR-gfp* (pZEMB25), P_{lac0-1}-
453 *asdI-gfp* (pZEMB26) and P_{lac0-1}-*asdI-II-gfp* (pZEMB27) were constructed by restriction
454 cloning into pZEMB8 using KpnI and EcoRI restriction endonucleases.
455 **Media and reagents.** Bacteria were cultured in Luria-Bertani (LB) broth medium or LB
456 agar plates (35) at 37°C, unless stated otherwise. Bacteria were grown in MOPS
457 (morpholine-propanesulfonic acid) rich defined medium (Teknova) with 0.2% fructose
458 for reporter fluorescence assays. When necessary, media were supplemented with
459 antibiotics at the following concentrations: 100 μg/ml ampicillin (Amp), 25 μg/ml
460 chloramphenicol (Cm), 25 μg/ml kanamycin (Kan) and 50 μg/ml spectinomycin (Spec).

Isopropyl β-D-1-thiogalactopyranoside (IPTG) was used at concentrations of 0.1-1.5 mM for induction of P_{lac0-1} promoter, anhydrotetracycline (aTc) was used at 0-50 ng/ml for induction of P_{tet0-1} promoter and L-arabinose was used at 0.000002%-0.2% for induction of P_{BAD} promoter, unless otherwise noted. To induce glucose-phosphate stress, 0.5% α-methylglucoside (αMG) was added to the growth medium.

Reporter fluorescence assay. Bacterial strains were cultured overnight in MOPS rich medium supplemented with 0.2% fructose, Amp, and Cm, and diluted 1:100 into fresh medium with appropriate inducers (IPTG, aTc) in 48 well plates. Relative fluorescence units (RFU) and optical density (OD_{600}) were measured over time. “GFP expression” was calculated by plotting RFU over OD_{600} and determining the slopes of linear regression plots for each IPTG concentration in exponentially growing cells in the presence of aTc to induce SgrS expression. “Promoter activity” was calculated by plotting RFU over OD_{600} and determining the slopes of linear regression plots for each IPTG concentration in exponentially growing cells in the absence of aTc.

***In vitro* transcription and radiolabeling**. Template DNA for *in vitro* transcription was generated by PCR using gene-specific oligonucleotides containing the T7 RNA polymerase promoter sequence. The following oligonucleotides were used to generate specific template DNA: MBP84F/MBP213R–*ptsG* (+1 to +240), O-JH218/MBP214R–*manX* (+1 to +240), MBP56F/MBP215R–*asdI-II* (+1 to +240), MBP56F/MBP222R–*asdI* (+1 to +110), MBP226F/MBP226R–*asdII* (+71 to +310), MBP65F/MBP174R–*purR* (+1 to +230), MBP216F/MBP216R–*yigL* (-191 to +50 relative to ATG translation start of *yigL*) MBP234F/MBP234R–*gfp* (+1 to +240) and O-JH219/O-JH119 were used to generate full-length *sgrS* template DNA. *In vitro* transcription of DNA templates was

484 performed according to specifications of the MEGAscript T7 Kit (Ambion). *In vitro*
485 transcribed RNA was 5'-end labeled with radioisotope ^{32}P using the KinaseMax Kit
486 (Ambion), according to the manufecturer's instructions. Samples were purified by
487 passing through Illustra ProbeQuant G-50 Micro Columns (GE Healthcare) followed by
488 extraction with phenol-chloroform:isoamyl alcohol (Ambion), and labeled RNA was
489 precipitated with ethanol:3M NaAc (30:1).
490 **RNA-RNA gel electrophoretic mobility shift assay**. Different concentrations of
491 unlabeled mRNA were mixed with 0.02 pmol of 5'-end labeled SgrS. Samples were
492 denatured at 95°C for 1 min, placed on ice for 5 min, and incubated at 37°C for 30 min
493 in 1x binding buffer (20 mM Tris-HCL [pH 8.0], 1mM DTT, 1 mM $MgCl_2$, 20 mM KCl, 10
494 mM Na_2HPO_4 [pH 8.0]) (39). Non-denaturing loading buffer was added and samples
495 were resolved for 6 h at 40 V on native 5.6% PAGE.
496 **Protein-RNA gel electrophoretic mobility shift assay.** 0.02 pmol of 5'-end labeled
497 mRNA was denatured at 95°C for 1 min, and placed on ice for 5 min. Different
498 concentrations of purified Hfq protein (His-tagged) were added. Samples were
499 incubated at 37°C for 30 min in 1x binding buffer. Non-denaturing loading buffer was
500 added and samples were resolved for 90 min at 20 mA on native 4.0% PAGE (39).
501 **SHAPE.** The *asdI-II* RNA (0.15 µM) and SgrS RNA (0.075 µM, 0.15 µM, 0.30 µM, 0.75
502 µM, 1.5 µM, or 3.0 µM) were folded separately as in (40) using a modified SHAPE
503 buffer (100 mM HEPES [pH 8.0], 2 mM $MgCl_2$, 40 mM NaCl). For each SgrS
504 concentration, the SgrS RNA or the equivalent volume of 0.5X TE was added to the
505 *asdI-II* RNA and the samples were incubated at 37°C for 30 min. The RNAs were
506 modified with *N*-methylisatoic anhydride (NMIA, 6.5 mM; Sigma-Aldrich) and collected

by ethanol precipitation as in (40). Parallel primer extension inhibition and sequencing reactions were performed using fluorescently labeled primers complementary to the 3' end of the *asdI-II* RNA (5′-AGATCAAAGGCATCCTGAAG, 22.5 nM; Applied Biosystems, ThermoFisher Scientific) as in (41) with minor modifications. Prior to primer binding, the RNAs were denatured and snap cooled and the reactions were carried out for 20 min at 52˚C, followed by 5 min at 65˚C. The cDNAs were analyzed on a 3730 DNA Analyzer (Applied Biosystems, Inc.). The data were processed and SHAPE reactivity (difference between the frequency of primer extension products at each nucleotide in +NMIA vs. -NMIA samples) was derived using the QuShape software (42). Data for each nucleotide were averaged with statistical outliers removed and normalized using the 2-8% rule (43). Relative reactivity was calculated by subtracting normalized SHAPE reactivity in the absence of the SgrS RNA from reactivity in the presence of the WT or MT SgrS RNA.

Single-molecule fluorescence *in situ* hybridization (smFISH). The *asdI-lacZ* (MB170), *asdII-lacZ* (MB183) and *asdI-II-lacZ* (MB171) strains were grown overnight at 37ºC with shaking at 250 rpm in LB Broth Miller (EMD) containing Kan and Spec. The next day, the overnight cultures were diluted 100-fold into MOPS EZ rich defined medium (Teknova) with 0.2% (w/w) sodium succinate, 0.02% glycerol and L-arabinose (0.01% for the *asdI-lacZ* and *asdII-lacZ* strains, 0.002% for *asdI-II-lacZ*) and were allowed to grow at 37ºC till the OD_{600} reached 0.15-0.25. αMG was added to the culture to a desired concentration to introduce sugar phosphate stress and induce SgrS sRNA expression. After 10 min of induction, the cells were fixed by mixing with formaldehyde (Fisher Scientific) at a final concentration of 4%.

530 Δ*sgrS* and Δ*lacZ* strains were grown in LB Broth Miller (EMD) at 37ºC with
531 shaking at 250 rpm overnight. The cultures were diluted 100-fold into MOPS EZ rich
532 defined medium (Teknova) with 0.2% glucose and allowed to grow at 37ºC until the
533 OD_{600} reached 0.2. The cells were then fixed by mixing with formaldehyde at a final
534 concentration of 4%. TK310 cells were grown overnight, similar to the knockout strains.
535 The overnight culture was then diluted 100-fold into MOPS EZ rich defined medium
536 (Teknova) with 0.2% glucose and 1 mM isopropyl β-D-1-thiogalactopyranoside (IPTG,
537 Sigma-Aldrich) and allowed to grow at 37ºC for 30 minutes. The cells were then fixed as
538 described above.
539 The fixation and permeabilization of the cells were done using the methods
540 published previously (44). After fixing with 4% formaldehyde, the cells were incubated at
541 room temperature for 30 min. The cells were then centrifuged at 600 x g for 7 min and
542 the pellets were washed with three times with 1X PBS 3. The cells were then
543 permeabilized with 70% ethanol for 1 h at room temperature and stored at 4ºC before
544 fluorescence *in situ* hybridization.
545 The smFISH probes were designed using Stellaris Probe Designer and
546 purchased from Biosearch Technologies (https://www.biosearchtech.com/). The labeling
547 of the probes was performed using equal volumes of each probe. The final volume of
548 sodium bicarbonate was adjusted to 0.1 M by adding 1/9 reaction volume of 1 M sodium
549 bicarbonate (pH = 8.5). The probe solution was mixed with 0.05-0.25 mg of Alexa Fluor
550 647 or Alexa Fluor 568 succinimidyl ester (Life Technologies) dissolved in 5 µL DMSO.
551 The dye was kept at 20-25 fold in molar excess relative to the probes. After incubation
552 with gentle vortexing in the dark at 37ºC overnight, the reaction was quenched by

553 adding 1/9 reaction volume of 3 M sodium acetate (pH 5). Unconjugated dye was
554 removed by ethanol precipitation followed by P-6 Micro Bio-Spin Column (Bio-Rad).
555 A previously published protocol (44) was used for the hybridization procedure. 60
556 µl of permeabilized cells were washed with FISH wash solution (10% formamide in 2X
557 SSC [Saline Sodium Citrate] buffer) and resuspended in 15 µl hybridization buffer (10%
558 dextran sulfate, 1 mg/ml *E. coli* tRNA, 0.2 mg/ml BSA, 2 mM vanadyl ribonucleoside
559 complexes, 10% formamide in 2X SSC) with probes. Nine probes labeled with Alexa
560 Fluor 647 were used for sRNA SgrS and 24 probes labeled with Alexa Fluor 568 were
561 used for mRNA *lacZ*. The concentration of the labeled probes for SgrS and *lacZ* mRNA
562 were 50 nM and 15 nM, respectively. The reactions were incubated in the dark at 3 ºC
563 overnight. The cells were then resuspended in 20X volume FISH wash solution and
564 centrifuged. They were then resuspended in FISH wash solution, incubated for 30 min
565 at 30ºC and centrifuged and this was repeated 3 times. The cells were pelleted after the
566 final washing step and resuspended in 20 µl 4X SSC and stored at 4ºC for imaging. The
567 labeled cells were immobilized on a poly-L-lysine (Sigma-Aldrich) treated 1.0
568 borosilicate chambered coverglass (Thermo Scientific™ Nunc™ Lab-Tek™). They were
569 then imaged in imaging buffer (50 mM Tris-HCl [pH = 8.0], 10% glucose, 1% β-
570 mercaptoethanol [Sigma-Aldrich], 0.5 mg/ml glucose oxidase [Sigma-Aldrich] and 0.2%
571 catalase [Calbiochem] in 2X SSC).
572 **Single-molecule localization-based super-resolution imaging.** An Olympus IX-71
573 inverted microscope with a 100X NA 1.4 SaPo oil immersion objective was used for the
574 3D super-resolution imaging. The lasers used for two-color imaging were Sapphire 568-
575 100 CW CDRH, Coherent (568nm) and DL640-100-AL-O, Crystalaser (647nm) and

576 DL405-025. Crystalaser (405nm) was used for the reactivation of Alexa 647 and Alexa
577 568 fluorophores. The laser excitation was controlled using mechanical shutters
578 (LS6T2, Uniblitz). A dichroic mirror (Di01-R405/488/561/635, Semrock) was used to
579 reflect the laser lines to the objective. The objective collected the emission signals and
580 then they made their way through an emission filter (FF01-594/730-25, Semrock for
581 Alexa 647 or HQ585/70M 63061, Chroma for Alexa 568) and excitation laser was
582 cleaned up using notch filters (ZET647NF, Chroma, NF01-568/647-25x5.0 and NF01-
583 568U-25, Semrock). Samples were then imaged on a 512x512 Andor EMCCD camera
584 (DV887ECS-BV, Andor Tech). Astigmatism was introduced by placing a cylindrical lens
585 with a focal length of 2 m (SCX-50.8-1000.0-UV-SLMF-520-820, CVI Melles Griot) in
586 the emission path between two relay lenses with focal lengths of 100 mm and 150 mm
587 each, which facilitated 3D imaging. In this setup, each pixel corresponded to 100 nm.
588 We used the CRISP (Continuous Reflective Interface Sample Placement) system (ASI)
589 to keep the z-drift of the setup to a minimum. The image acquisition was controlled
590 using the storm-control software written in Python by Zhuang and coworkers (45, 46)
591 and available at GitHub.
592 The imaging of the sample began with a DIC image of the sample area.
593 Subsequently two-color super-resolution imaging was performed. 647nm excitation was
594 used first and after image acquisition was completed for Alexa Fluor 647, 568nm
595 excitation was used to image Alexa Fluor 568. 405 nm laser power was increased
596 slowly to compensate for fluorophore bleaching and also to maintain moderate signal
597 density. Imaging was stopped when most of the fluorophores had photobleached and
598 the highest reactivation laser power was reached.

599 The raw data acquired using the acquisition software were analyzed using the
600 method described in previously published work (29), which was a modification of the
601 algorithm published by Zhuang and coworkers (45, 46). The clustering analysis on the
602 localization data was performed using MATLAB codes as described previously (29).
603 Background signal was estimated using Δ*sgrS* and Δ*lacZ* strains and they were
604 prepared, imaged and analyzed as described above. TK310 cells were prepared,
605 imaged and analyzed in the same way as a low copy *lacZ* mRNA sample for copy
606 number calculation. The copy number calculation was also performed using MATLAB
607 codes as described previously (29).

608 **ACKNOWLEDGEMENTS**

609 We would like to extend a special thank you to Erel Levine for providing
610 plasmids. We are grateful to Jennifer Rice, Rich Yemm, Divya Balasubramanian,
611 Chelsea Lloyd, Alisa King, Jessica Kelliher and other current and past members of the
612 Vanderpool lab for strains, plasmids and valuable advice. We appreciate and thank
613 Prof. James Slauch and members of his lab for fruitful discussions.

614 **FUNDING**

615 National Institutes of Health R01 GM092830 (M.B. and C.K.V.), R01 GM112659 (M.B.,
616 M.S.A., T.H., J.Z., and A.P.), R35 GM122569 (T.H., J.Z., and A.P.), R01 GM047823
617 (T.M.H.), T32 GM086252 (J.K.F.); National Science Foundation PHY 1430124 (T.H.,
618 J.Z., and A.P); University of Illinois Department of Microbiology James R. Beck
619 Fellowship (M.B.).

620

REFERENCES

1. Fang FC, Frawley ER, Tapscott T, Vazquez-Torres A. 2016. Bacterial stress responses during host infection. Cell Host Microbe 20:133-43.
2. Georg J, Hess W. 2011. *Cis*-antisense RNA, another level of gene regulation in bacteria. Microbiology and molecular biology reviews : MMBR 75:286-300.
3. Storz G, Vogel J, Wassarman KM. 2011. Regulation by small RNAs in bacteria: expanding frontiers. Mol Cell 43:880-91.
4. Carroll RK, Weiss A, Broach WH, Wiemels RE, Mogen AB, Rice KC, Shaw LN. 2016. Genome-wide annotation, identification, and global transcriptomic analysis of regulatory or Small RNA Gene Expression in Staphylococcus aureus. MBio 7:e01990-15.
5. Koo JT, Lathem WW. 2012. Global discovery of small noncoding RNAs in pathogenic *Yersinia* species. Adv Exp Med Biol 954:305-14.
6. Zhang A, Wassarman KM, Rosenow C, Tjaden BC, Storz G, Gottesman S. 2003. Global analysis of small RNA and mRNA targets of Hfq. Mol Microbiol 50:1111-24.
7. Salvail H, Masse E. 2012. Regulating iron storage and metabolism with RNA: an overview of posttranscriptional controls of intracellular iron homeostasis. Wiley Interdiscip Rev RNA 3:26-36.
8. Sharma CM, Papenfort K, Pernitzsch SR, Mollenkopf HJ, Hinton JC, Vogel J. 2011. Pervasive post-transcriptional control of genes involved in amino acid metabolism by the Hfq-dependent GcvB small RNA. Mol Microbiol 81:1144-65.
9. Bobrovskyy M, Vanderpool CK. 2013. Regulation of bacterial metabolism by small RNAs using diverse mechanisms. Annu Rev Genet 47:209-32.
10. Bobrovskyy M, Vanderpool CK, Richards GR. 2015. Small RNAs regulate primary and secondary metabolism in gram-negative bacteria. Microbiol Spectr 3.
11. Vanderpool CK, Gottesman S. 2004. Involvement of a novel transcriptional activator and small RNA in post-transcriptional regulation of the glucose phosphoenolpyruvate phosphotransferase system. Mol Microbiol 54:1076-89.
12. Vanderpool CK, Gottesman S. 2007. The novel transcription factor SgrR coordinates the response to glucose-phosphate stress. J Bacteriol 189:2238-48.
13. Rice JB, Balasubramanian D, Vanderpool CK. 2012. Small RNA binding-site multiplicity involved in translational regulation of a polycistronic mRNA. Proc Natl Acad Sci U S A 109:E2691-8.
14. Rice JB, Vanderpool CK. 2011. The small RNA SgrS controls sugar-phosphate accumulation by regulating multiple PTS genes. Nucleic Acids Res 39:3806-19.
15. Papenfort K, Sun Y, Miyakoshi M, Vanderpool CK, Vogel J. 2013. Small RNA-mediated activation of sugar phosphatase mRNA regulates glucose homeostasis. Cell 153:426-37.
16. Bobrovskyy M, Vanderpool CK. 2016. Diverse mechanisms of post-transcriptional repression by the small RNA regulator of glucose-phosphate stress. Mol Microbiol 99:254-73.
17. Chevance FF, Hughes KT. 2008. Coordinating assembly of a bacterial macromolecular machine. Nat Rev Microbiol 6:455-65.
18. Syed KA, Beyhan S, Correa N, Queen J, Liu J, Peng F, Satchell KJ, Yildiz F, Klose KE. 2009. The *Vibrio cholerae* flagellar regulatory hierarchy controls expression of virulence factors. J Bacteriol 191:6555-70.
19. Tonner PD, Pittman AM, Gulli JG, Sharma K, Schmid AK. 2015. A regulatory hierarchy controls the dynamic transcriptional response to extreme oxidative stress in archaea. PLoS Genet 11:e1004912.
20. Yu H, Gerstein M. 2006. Genomic analysis of the hierarchical structure of regulatory networks. Proc Natl Acad Sci U S A 103:14724-31.

21. Gao R, Stock AM. 2015. Temporal hierarchy of gene expression mediated by transcription factor binding affinity and activation dynamics. MBio 6:e00686-15.
22. Feng L, Rutherford ST, Papenfort K, Bagert JD, van Kessel JC, Tirrell DA, Wingreen NS, Bassler BL. 2015. A qrr noncoding RNA deploys four different regulatory mechanisms to optimize quorum-sensing dynamics. Cell 160:228-40.
23. Levine E, Zhang Z, Kuhlman T, Hwa T. 2007. Quantitative characteristics of gene regulation by small RNA. PLoS Biol 5:e229.
24. Busch A, Richter AS, Backofen R. 2008. IntaRNA: efficient prediction of bacterial sRNA targets incorporating target site accessibility and seed regions. Bioinformatics 24:2849-56.
25. Wright PR, Georg J, Mann M, Sorescu DA, Richter AS, Lott S, Kleinkauf R, Hess WR, Backofen R. 2014. CopraRNA and IntaRNA: predicting small RNA targets, networks and interaction domains. Nucleic Acids Res 42:W119-23.
26. Morita T, Kawamoto H, Mizota T, Inada T, Aiba H. 2004. Enolase in the RNA degradosome plays a crucial role in the rapid decay of glucose transporter mRNA in the response to phosphosugar stress in *Escherichia coli*. Mol Microbiol 54:1063-75.
27. Morita T, Maki K, Aiba H. 2005. RNase E-based ribonucleoprotein complexes: mechanical basis of mRNA destabilization mediated by bacterial noncoding RNAs. Genes Dev 19:2176-86.
28. Kawamoto H, Koide Y, Morita T, Aiba H. 2006. Base-pairing requirement for RNA silencing by a bacterial small RNA and acceleration of duplex formation by Hfq. Mol Microbiol 61:1013-22.
29. Fei J, Singh D, Zhang Q, Park S, Balasubramanian D, Golding I, Vanderpool CK, Ha T. 2015. RNA biochemistry. Determination of *in vivo* target search kinetics of regulatory noncoding RNA. Science 347:1371-4.
30. Morita T, Mochizuki Y, Aiba H. 2006. Translational repression is sufficient for gene silencing by bacterial small noncoding RNAs in the absence of mRNA destruction. Proc Natl Acad Sci U S A 103:4858-63.
31. Moon K, Gottesman S. 2011. Competition among Hfq-binding small RNAs in *Escherichia coli*. Mol Microbiol 82:1545-62.
32. Santiago-Frangos A, Kavita K, Schu DJ, Gottesman S, Woodson SA. 2016. C-terminal domain of the RNA chaperone Hfq drives sRNA competition and release of target RNA. Proc Natl Acad Sci U S A 113:E6089-E6096.
33. Schu DJ, Zhang A, Gottesman S, Storz G. 2015. Alternative Hfq-sRNA interaction modes dictate alternative mRNA recognition. EMBO J 34:2557-73.
34. Sun Y, Vanderpool CK. 2011. Regulation and function of *Escherichia coli* sugar efflux transporter A (SetA) during glucose-phosphate stress. J Bacteriol 193:143-53.
35. Miller JH. 1972. Experiments in bacterial genetics. Cold Spring Harbor Laboratory Press, Cold Spring Harbor, NY.
36. Datsenko KA, Wanner BL. 2000. One-step inactivation of chromosomal genes in *Escherichia coli* K-12 using PCR products. Proc Natl Acad Sci U S A 97:6640-5.
37. Yu D, Ellis HM, Lee EC, Jenkins NA, Copeland NG, Court DL. 2000. An efficient recombination system for chromosome engineering in *Escherichia coli*. Proc Natl Acad Sci U S A 97:5978-83.
38. Corcoran CP, Podkaminski D, Papenfort K, Urban JH, Hinton JC, Vogel J. 2012. Superfolder GFP reporters validate diverse new mRNA targets of the classic porin regulator, MicF RNA. Mol Microbiol 84:428-45.
39. Morita T, Maki K, Aiba H. 2012. Detection of sRNA-mRNA interactions by electrophoretic mobility shift assay. Methods Mol Biol 905:235-44.

719 40. Wilkinson KA, Merino EJ, Weeks KM. 2006. Selective 2'-hydroxyl acylation analyzed by
720 primer extension (SHAPE): quantitative RNA structure analysis at single nucleotide
721 resolution. Nat Protoc 1:1610-6.
722 41. Mortimer SA, Weeks KM. 2009. Time-resolved RNA SHAPE chemistry: quantitative
723 RNA structure analysis in one-second snapshots and at single-nucleotide resolution. Nat
724 Protoc 4:1413-21.
725 42. Karabiber F, McGinnis JL, Favorov OV, Weeks KM. 2013. QuShape: rapid, accurate,
726 and best-practices quantification of nucleic acid probing information, resolved by
727 capillary electrophoresis. RNA 19:63-73.
728 43. McGinnis JL, Duncan CD, Weeks KM. 2009. High-throughput SHAPE and hydroxyl
729 radical analysis of RNA structure and ribonucleoprotein assembly. Methods Enzymol
730 468:67-89.
731 44. So LH, Ghosh A, Zong C, Sepulveda LA, Segev R, Golding I. 2011. General properties
732 of transcriptional time series in *Escherichia coli*. Nat Genet 43:554-60.
733 45. Rust MJ, Bates M, Zhuang X. 2006. Sub-diffraction-limit imaging by stochastic optical
734 reconstruction microscopy (STORM). Nat Methods 3:793-5.
735 46. Huang B, Wang W, Bates M, Zhuang X. 2008. Three-dimensional super-resolution
736 imaging by stochastic optical reconstruction microscopy. Science 319:810-3.
737 47. Lorenz R, Luntzer D, Hofacker IL, Stadler PF, Wolfinger MT. 2016. SHAPE directed
738 RNA folding. Bioinformatics 32:145-7.
739 48. Ishikawa H, Otaka H, Maki K, Morita T, Aiba H. 2012. The functional Hfq-binding module
740 of bacterial sRNAs consists of a double or single hairpin preceded by a U-rich sequence
741 and followed by a 3' poly(U) tail. RNA 18:1062-74.
742

743 **FIGURE LEGENDS**

744 **Figure 1. Model for SgrS target prioritization during glucose-phosphate stress.**

745 Glucose or the analogs αMG and 2-deoxyglucose are phosphorylated during transport

746 through the phosphotransferase system proteins EIICB^{Glc} (PtsG) or EIICD^{Man} (ManYZ).

747 If sugar-phosphates are not metabolized, the glucose-phosphate stress response is

748 triggered, and the transcription factor SgrR becomes active and promotes *sgrS*

749 transcription. The RNA chaperone Hfq promotes SgrS-mediated translational repression

750 of *ptsG* and *manXYZ* mRNAs, reducing synthesis of sugar transporters. SgrS stabilizes

751 *yigL* mRNA, promoting sugar phosphatase (YigL) synthesis. SgrS-mediated repression

752 of *asd, purR, folE* and *adiY* likely reroutes metabolism to restore homeostasis during

753 stress recovery. The hypothetical sequence of regulatory events following stress

754 induction is represented from left to right as SgrS levels increase over time. When SgrS

concentrations are low, only the highest priority targets are regulated. When stress persists and concentrations of SgrS increase, lower priority targets are regulated.

Figure 2. Efficiency of target regulation by SgrS. A) Representation of genetic constructs in two compatible plasmids used to study target regulation by SgrS. One plasmid contains full-length SgrS under the control of the aTc-inducible P_{Tet} promoter. A second plasmid contains a P_{Lac} promoter and the relevant region encoding each SgrS target (including the SgrS binding site) translationally fused to a superfolder *gfp* reporter gene. B-F) Regulated activity was plotted as a function of basal activity (see text for description) for (B) *ptsG*, (C) *manX*, (D) *purR,* (E) *asdI,* and (F) *yigL* fused to *sfgfp* reporter gene. Without SgrS-mediated regulation, we obtained a line with a slope =1. The plots with slopes <1 indicate repression of (B) *ptsG*, (C) *manX*, (D) *purR* and (E) *asdI* by SgrS. The plot with a slope of >1 is indicative of activation of (F) *yigL*.

Figure 3. Regulatory hierarchy established by SgrS. Regulated activity was plotted as a function of basal activity for *ptsG*, *manX*, *purR, asdI,* and *yigL* fusions. Lack of SgrS regulation is indicated by a line with a slope =1. The plots with slopes <1 indicate repression (*ptsG*, *manX*, *purR* and *asdI*) by SgrS. The plot with slope >1 indicates activation (*yigL*). Target fusion activity was monitored at different levels of SgrS induction by aTc: (A) 10 ng/ml, (B) 20 ng/ml, (C) 30 ng/ml, (D) 40 ng/ml, (E) 50 ng/ml.

Figure 4. SgrS binding to target mRNAs *in vitro*. A) SgrS was labeled with ^{32}P and incubated with unlabeled target transcripts at final concentrations of 0 μM - 16 μM . Electrophoretic mobility shift assays (EMSAs) were performed after incubating full-length SgrS (+1 to +227) with its target transcripts (A) *ptsG* (+1 to +240), *manX* (+1 to +240), *purR* (+1 to +230), *yigL* (-191 to +50 relative to ATG translation start of *yigL*),

778 *asdI* (+1 to +110), and *asdII* (+71 to +310). B-D) Target transcripts (B) *ptsG* (+1 to
779 +240), (C) *manX* (+1 to +240), (D) *asdI* (+1 to +110) were labeled with ^{32}P and
780 incubated with unlabeled SgrS. EMSAs were performed to resolve complex formation.
781 Band densities were measured for replicate experiments (n, top left) and plotted to
782 determine dissociation constant (K_D, bottom right) values for (B) *ptsG*, (C) *manX*, and
783 (D) *asdI*. E) EMSA of radiolabeled SgrS in the presence of increasing concentrations of
784 *asdI-II* transcript. Shift in mobility corresponding to one or two SgrS bound to *asdI-II* is
785 denoted as Site I-SgrS* and Sites I-II-SgrS* respectively. F) Quantification of SgrS
786 binding with radiolabeled *asdI-II* (+1 to +240), as described above.
787 **Figure 5. Secondary structure of 5' end of *asd*.** A) Diagram showing base-pairing
788 interactions of SgrS with binding sites I and II of *asd* mRNA. B) Energy of interaction
789 predicted by IntaRNA (26). "Structured" indicates pairing between full length SgrS (+1 to
790 +227) and *asdI-II* (+1 to +180). Plotted is the energy of interactions at either site I (*asdI*)
791 or site II (*asdII*). "Isolated" indicates interactions between isolated binding sites: SgrS
792 (+158 to +176) with *asdI* (+31 to +49) and SgrS (+158 to +178) pairing with *asdII* (+110
793 to +129). C) The structure of the *asdI-II* RNA alone or in complex with SgrS was probed
794 with NMIA and the modified RNA was analyzed by primer extension inhibition. SHAPE
795 reactivity (difference between the frequency of primer extension products at each
796 nucleotide in +NMIA vs. -NMIA samples) was then used as a parameter in the Vienna
797 RNAprobing WebServer (47) to predict the secondary structure of the *asdI-II* RNA.
798 Colors indicate SHAPE reactivity as follows: red, highly reactive (≥ 0.8); gold, reactive
799 (0.4-0.79); green, moderately reactive (0.2-0.39); blue, minimally reactive (0.1-0.19);
800 grey, unreactive (< 0.01). Distinct structures were observed in the absence of SgrS and

in the presence of saturating concentrations of SgrS. The SHAPE reactivity of *asdI-II* RNA alone (left) or in the presence of 5-fold excess SgrS (right) is mapped to the predicted secondary structures. (D) SHAPE reactivity as a function of SgrS concentration for each binding site (top, site I; bottom, site II). Only nucleotides with a significant (≥ 0.1) change in reactivity are shown. Error bars denote SEM, n = 9. (E) Relative SHAPE reactivity (difference in the SHAPE reactivity in the presence of SgrS vs. the absence of SgrS) of the *asdI-II* RNA in the presence of wild-type (top) or mutant (bottom) SgrS. Error bars denote SEM, n = 9 (WT), 6 (MT). The *asdI-II* RNA nucleotides are numbered below the X-axis and the SgrS binding sites are indicated.

Figure 6. STORM imaging of SgrS regulation of *asd* variants. A) Illustration of *asdI-II*, *asdI* and *asdII* translationally fused to *lacZ* reporter with SgrS binding sites I and II marked. B-D) 2D projection of 3D super-resolution images of SgrS and *lacZ* mRNA for the different *asd-lacZ* variants, labeled by smFISH, before and after 10 min induction with 1% αMG. (B), (C) and (D) correspond to *asdI-lacZ*, *asdII-lacZ,* and *asdI-II-lacZ* shown in (A). Probability distributions of RNA copy numbers in individual cells for 30-250 cells are plotted next to the representative images.

Figure 7. SgrS binding cooperativity allows for improved repression of *asd* translation. A) Illustration of *asdI* and *asdI-II* constructs with SgrS binding sites marked. Graphs show comparison of SgrS regulation of *asdI* and *asdI-II* variants in (B) wild-type and (D) *rne701* mutant by plotting regulated activity over basal activity at various SgrS expression levels (20-100 ng/ml aTc). Regulatory hierarchy of SgrS targets in (C) wild-type and (E) *rne701* mutant strains. Regulation of target genes at one SgrS expression

823 level (40 ng/ml aTc) are compared by plotting regulated activity over basal activity of the
824 *gfp* reporter.

825 **Figure 8. SgrS regulation of transcriptional *asd-lacZ* fusions.** β-galactosidase
826 activity of (A) *asdI-lacZ* (+1 to +64) and *asdI-II-lacZ* (+1 to +277) was (B) assayed in
827 response to SgrS expression from a plasmid (and vector control) in WT and *rne701*
828 background strains.

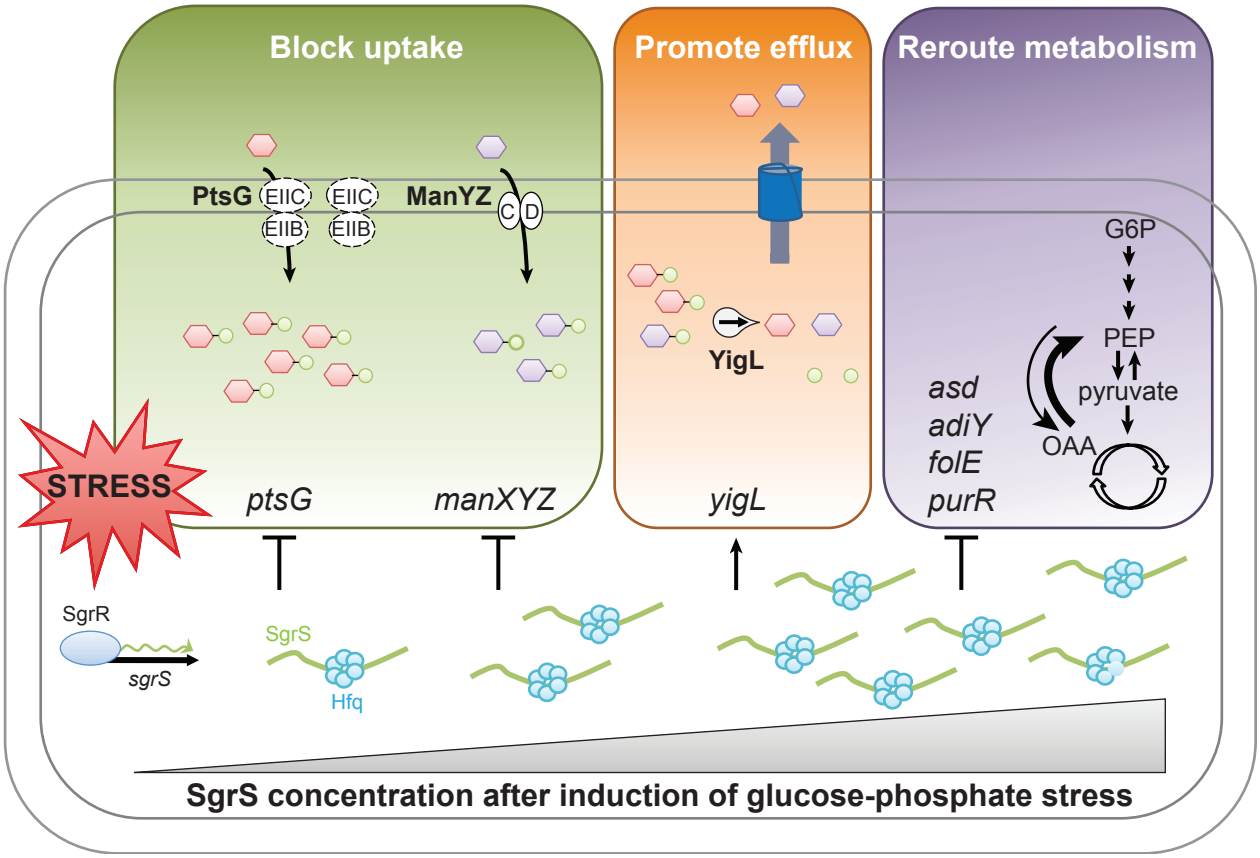

Figure 1. Model for SgrS target prioritization during glucose-phosphate stress. Glucose or the analogs αMG and 2-deoxyglucose are phosphorylated during transport through the phosphotransferase system proteins EIICB^{Glc} (PtsG) or EIICD^{Man} (ManYZ). If sugar-phosphates are not metabolized, the glucose-phosphate stress response is triggered, and the transcription factor SgrR becomes active and promotes *sgrS* transcription. The RNA chaperone Hfq promotes SgrS-mediated translational repression of *ptsG* and *manXYZ* mRNAs, reducing synthesis of sugar transporters. SgrS stabilizes *yigL* mRNA, promoting sugar phosphatase (YigL) synthesis. SgrS-mediated repression of *asd, purR, folE* and *adiY* likely reroutes metabolism to restore homeostasis during stress recovery. The hypothetical sequence of regulatory events following stress induction is represented from left to right as SgrS levels increase over time. When SgrS concentrations are low, only the highest priority targets are regulated. When stress persists and concentrations of SgrS increase, lower priority targets are regulated.

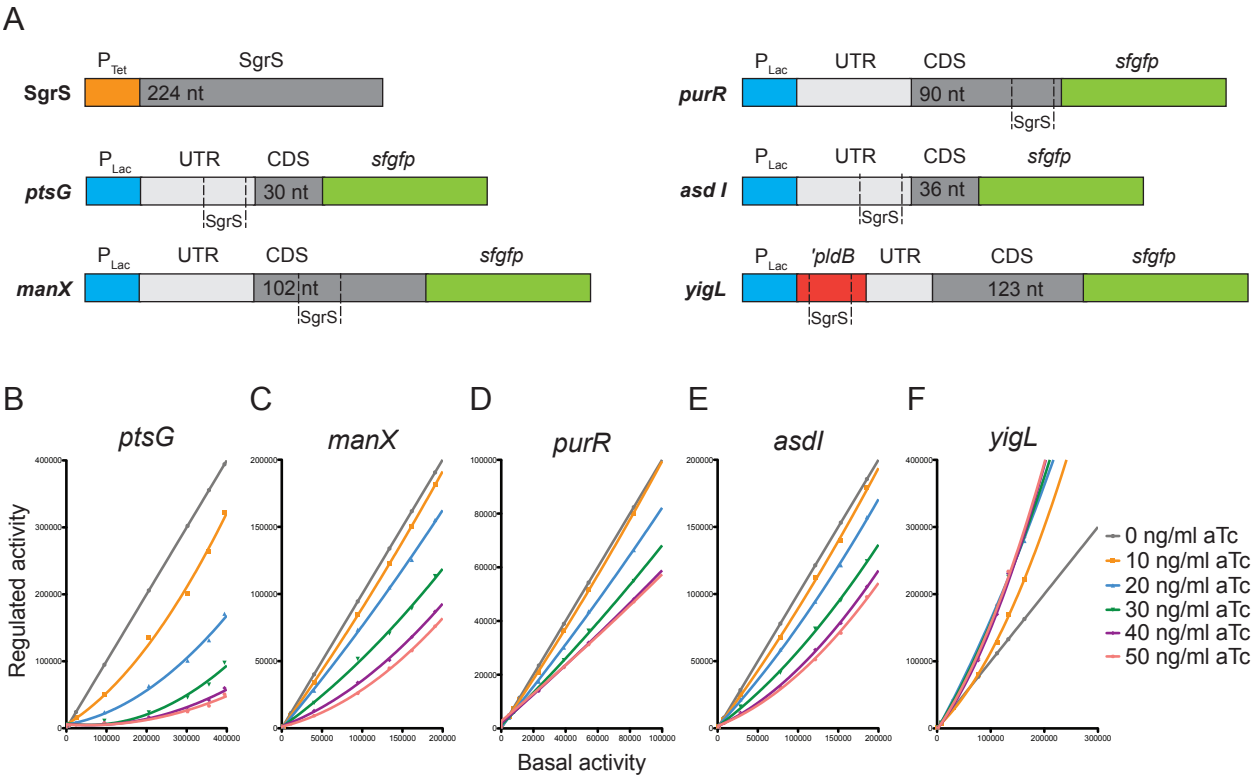

Figure 2. Efficiency of target regulation by SgrS. A) Representation of genetic constructs in two compatible plasmids used to study target regulation by SgrS. One plasmid contains full-length SgrS under the control of the aTc-inducible P_{Tet} promoter. A second plasmid contains a P_{Lac} promoter and the relevant region encoding each SgrS target (including the SgrS binding site) translationally fused to a superfolder *gfp* reporter gene. B-F) Regulated activity was plotted as a function of basal activity (see text for description) for (B) *ptsG*, (C) *manX*, (D) *purR,* (E) *asdI,* and (F) *yigL* fused to *sfgfp* reporter gene. Without SgrS-mediated regulation, we obtained a line with a slope =1. The plots with slopes <1 indicate repression of (B) *ptsG*, (C) *manX*, (D) *purR* and (E) *asdI* by SgrS. The plot with a slope of >1 is indicative of activation of (F) *yigL*.

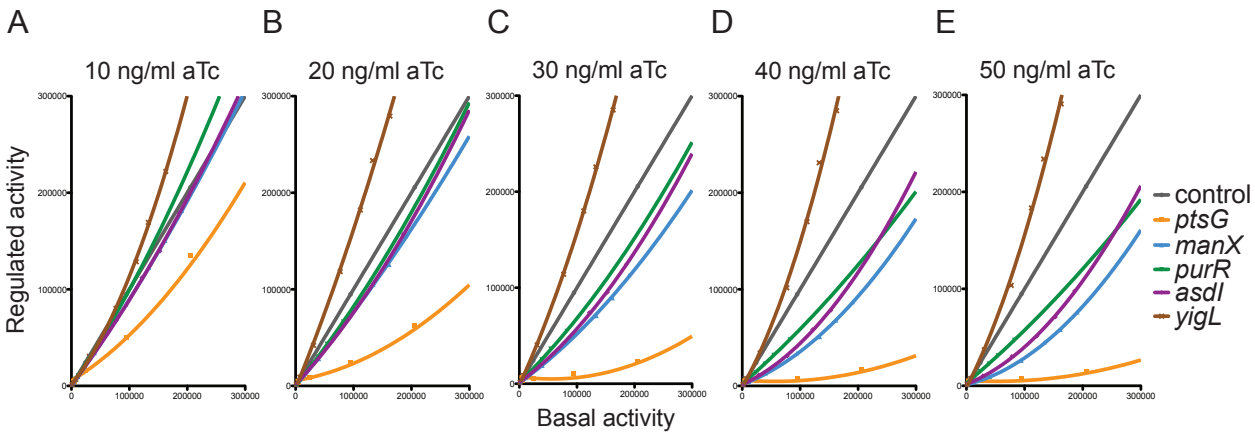

Figure 3. Regulatory hierarchy established by SgrS. Regulated activity was plotted as a function of basal activity for *ptsG*, *manX*, *purR, asdI,* and *yigL* fusions. Lack of SgrS regulation is indicated by a line with a slope =1. The plots with slopes <1, indicate repression (*ptsG*, *manX*, *purR* and *asdI*) by SgrS. The plot with slope >1 indicates activation (*yigL*). Target fusion activity was monitored at different levels of SgrS induction by aTc: (A) 10 ng/ml, (B) 20 ng/ml, (C) 30 ng/ml, (D) 40 ng/ml, (E) 50 ng/ml.

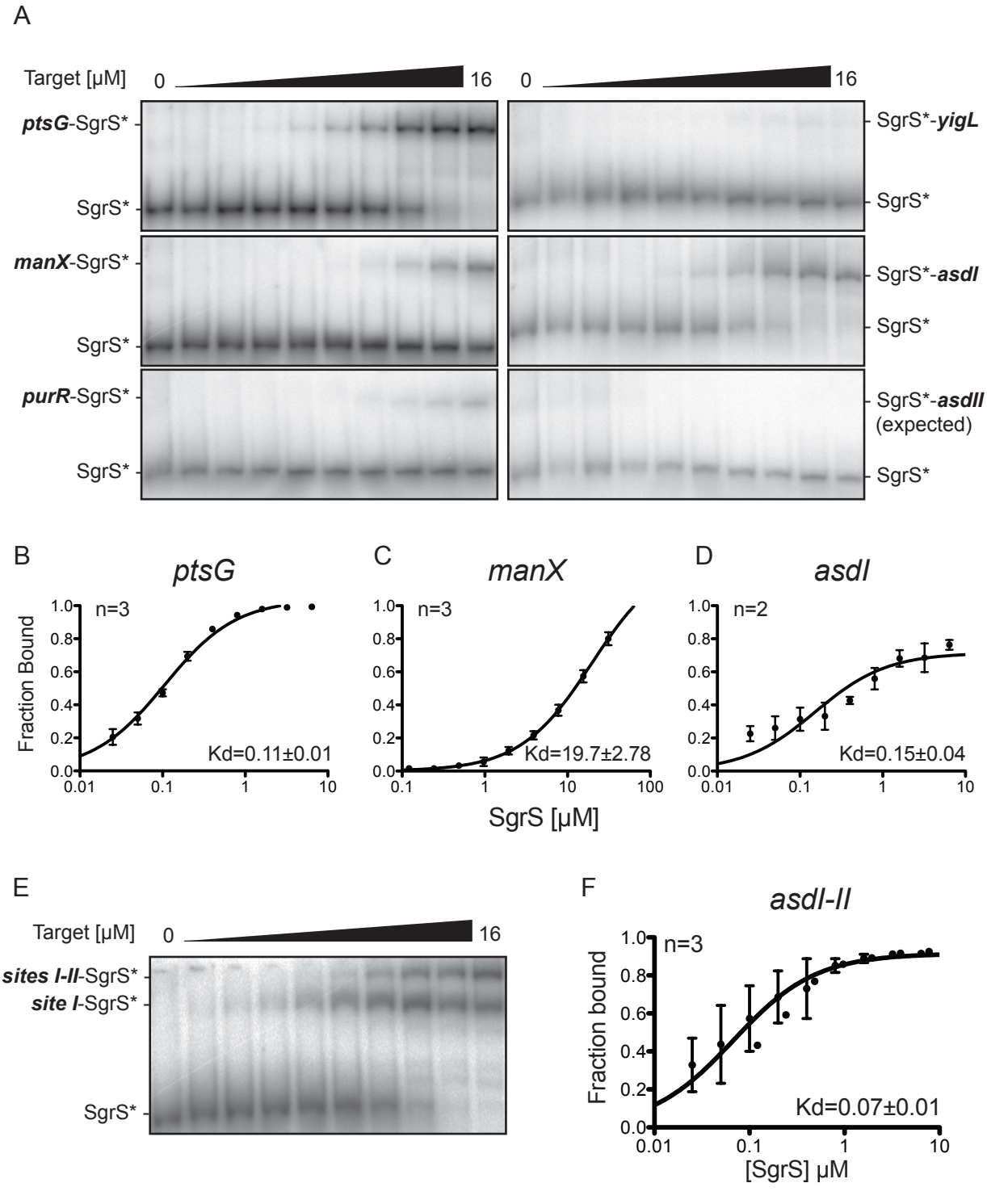

Figure 4 legend on the next page

Figure 4. SgrS binding to target mRNAs *in vitro*. A) SgrS was labeled with ^{32}P and incubated with unlabeled target transcripts at final concentrations of 0 μM - 16 μM . Electrophoretic mobility shift assays (EMSAs) were performed after incubating full-length SgrS (+1 to +227) with its target transcripts (A) *ptsG* (+1 to +240), *manX* (+1 to +240), *purR* (+1 to +230), *yigL* (-191 to +50 relative to ATG translation start of *yigL*), *asdI* (+1 to +110), and *asdII* (+71 to +310). B-D) Target transcripts (B) *ptsG* (+1 to +240), (C) *manX* (+1 to +240), (D) *asdI* (+1 to +110) were labeled with ^{32}P and incubated with unlabeled SgrS. EMSAs were performed to resolve complex formation. Band densities were measured for replicate experiments (n, top left) and plotted to determine dissociation constant (K_D, bottom right) values for (B) *ptsG*, (C) *manX*, and (D) *asdI*. E) EMSA of radiolabeled SgrS in the presence of increasing concentrations of *asdI-II* transcript. Shift in mobility corresponding to one or two SgrS bound to *asdI-II* is denoted as Site I-SgrS* and Sites I-II-SgrS* respectively. F) Quantification of SgrS binding with radiolabeled *asdI-II* (+1 to +240), as described above.

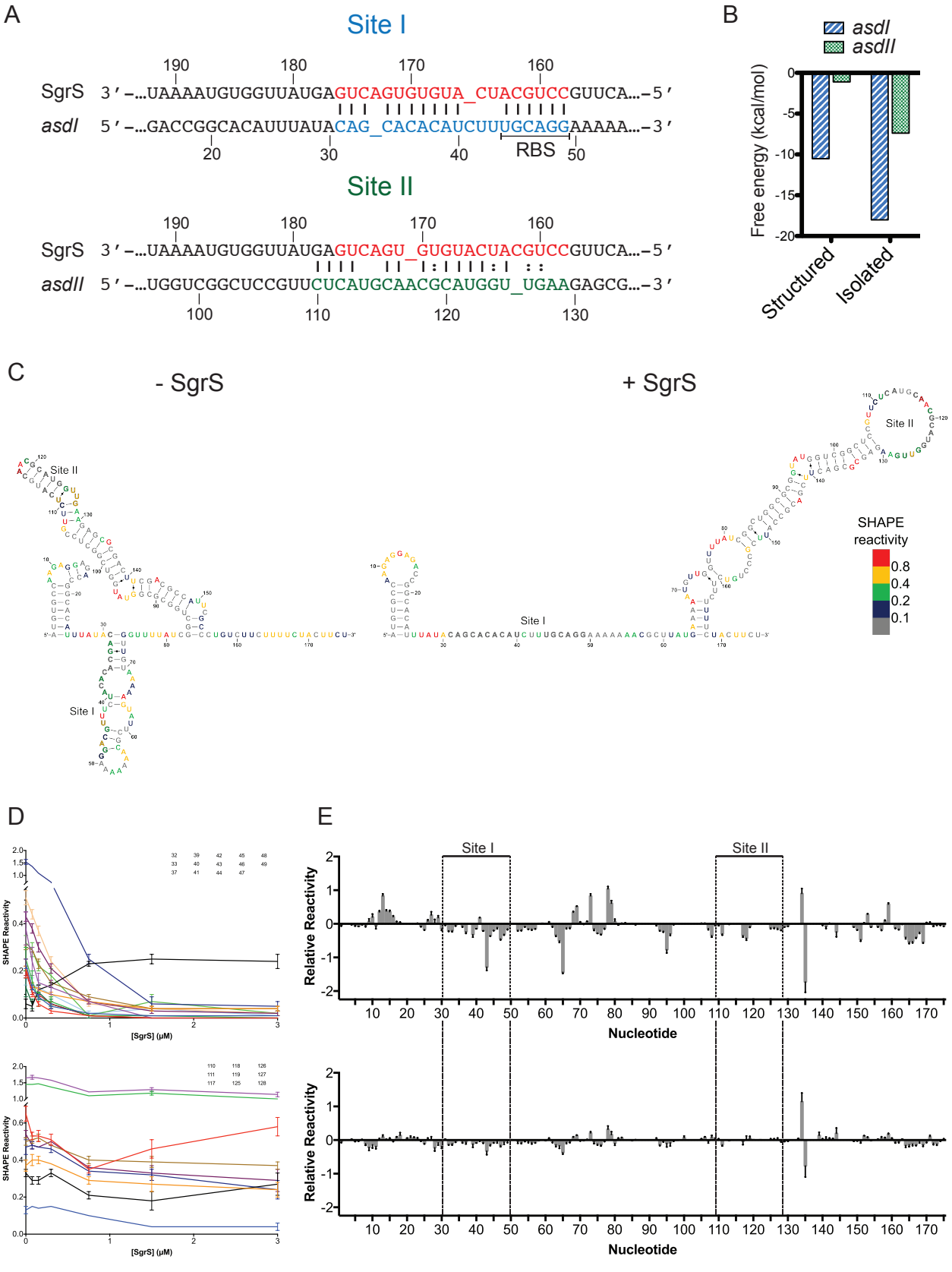

Figure 5 legend on the next page

Figure 5. Secondary structure of 5' end of *asd*. A) Diagram showing base-pairing interactions of SgrS with binding sites I and II of *asd* mRNA. B) Energy of interaction predicted by IntaRNA (26). "Structured" indicates pairing between full length SgrS (+1 to +227) and *asdI-II* (+1 to +180). Plotted is the energy of interactions at either site I (*asdI*) or site II (*asdII*). "Isolated" indicates interactions between isolated binding sites: SgrS (+158 to +176) with *asdI* (+31 to +49) and SgrS (+158 to +178) pairing with *asdII* (+110 to +129). C) The structure of the *asdI-II* RNA alone or in complex with SgrS was probed with NMIA and the modified RNA was analyzed by primer extension inhibition. SHAPE reactivity (difference between the frequency of primer extension products at each nucleotide in +NMIA vs. -NMIA samples) was then used as a parameter in the Vienna RNAprobing WebServer (55) to predict the secondary structure of the *asdI-II* RNA. Colors indicate SHAPE reactivity as following: red, highly reactive (≥ 0.8); gold, reactive (0.4-0.79); green, moderately reactive (0.2-0.39); blue, minimally reactive (0.1-0.19); grey, unreactive (< 0.01). Distinct structures were observed in the absence of SgrS and in the presence of saturating concentrations of SgrS. The SHAPE reactivity of *asdI-II* RNA alone (left) or in the presence of 5-fold excess SgrS (right) is mapped to the predicted secondary structures. (D) SHAPE reactivity as a function of SgrS concentration for each binding site (top, site I; bottom, site II). Only nucleotides with a significant (≥ 0.1) change in reactivity are shown. Error bars denote SEM, n = 9. (E) Relative SHAPE reactivity (difference in the SHAPE reactivity in the presence of SgrS vs. the absence of SgrS) of the *asdI-II* RNA in the presence of wild-type (top) or mutant (bottom) SgrS. Error bars denote SEM, n = 9 (WT), 6 (MT). The *asdI-II* RNA nucleotides are numbered below the X-axis and the SgrS binding sites are indicated.

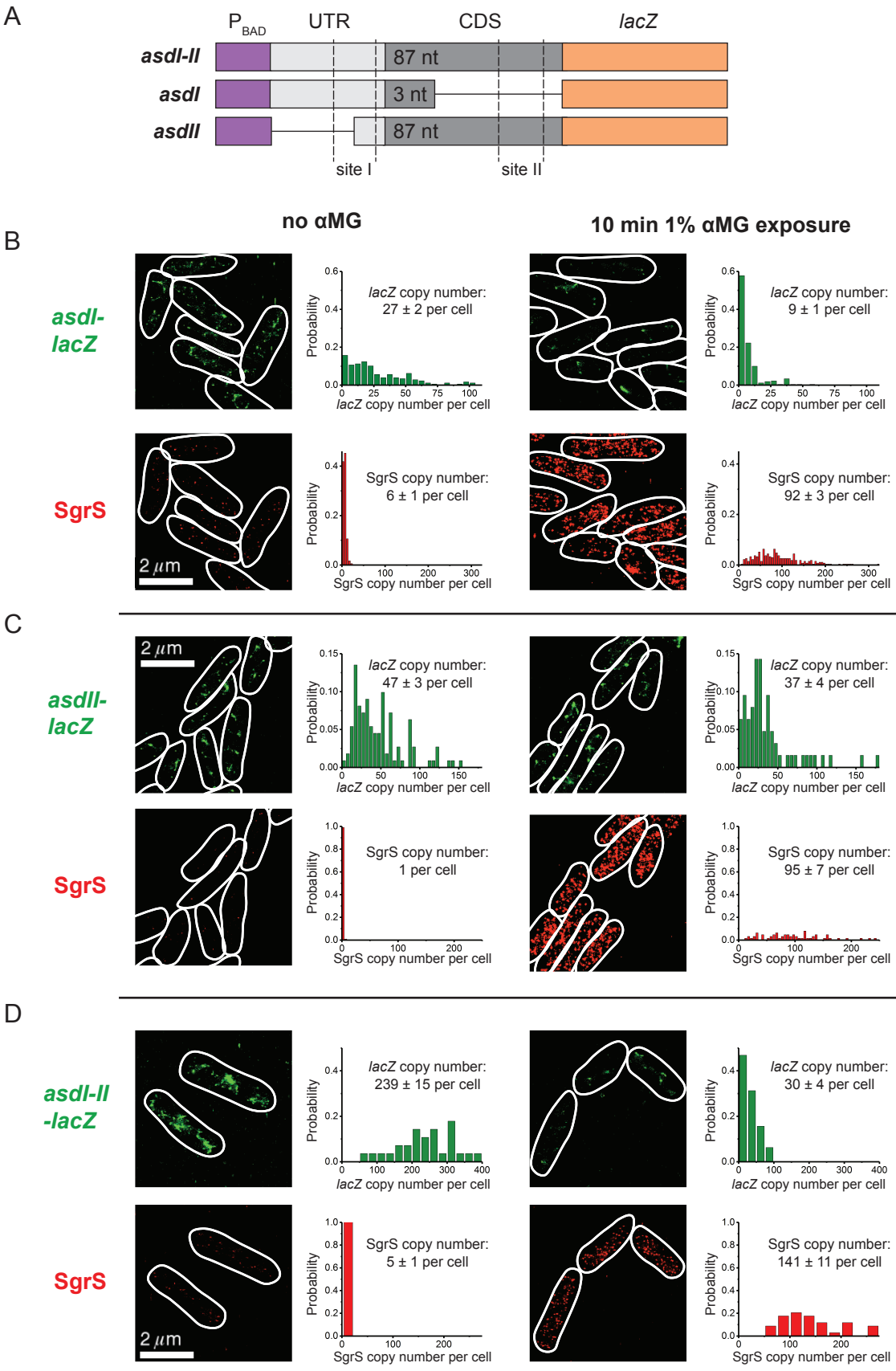

Figure 6 legend on the next page

Figure 6. STORM imaging of SgrS regulation of *asd* variants. A) Illustration of *asdI-II*, *asdI* and *asdII* translationally fused to *lacZ* reporter with SgrS binding sites I and II marked. B-D) 2D projection of 3D super-resolution images of SgrS and *lacZ* mRNA for the different *asd-lacZ* variants, labeled by smFISH, before and after 10 min induction with 1% αMG. (B), (C) and (D) correspond to *asdI-lacZ*, *asdII-lacZ,* and *asdI-II-lacZ* shown in (A). Probability distributions of RNA copy numbers in individual cells for 30-250 cells are plotted next to the representative images.

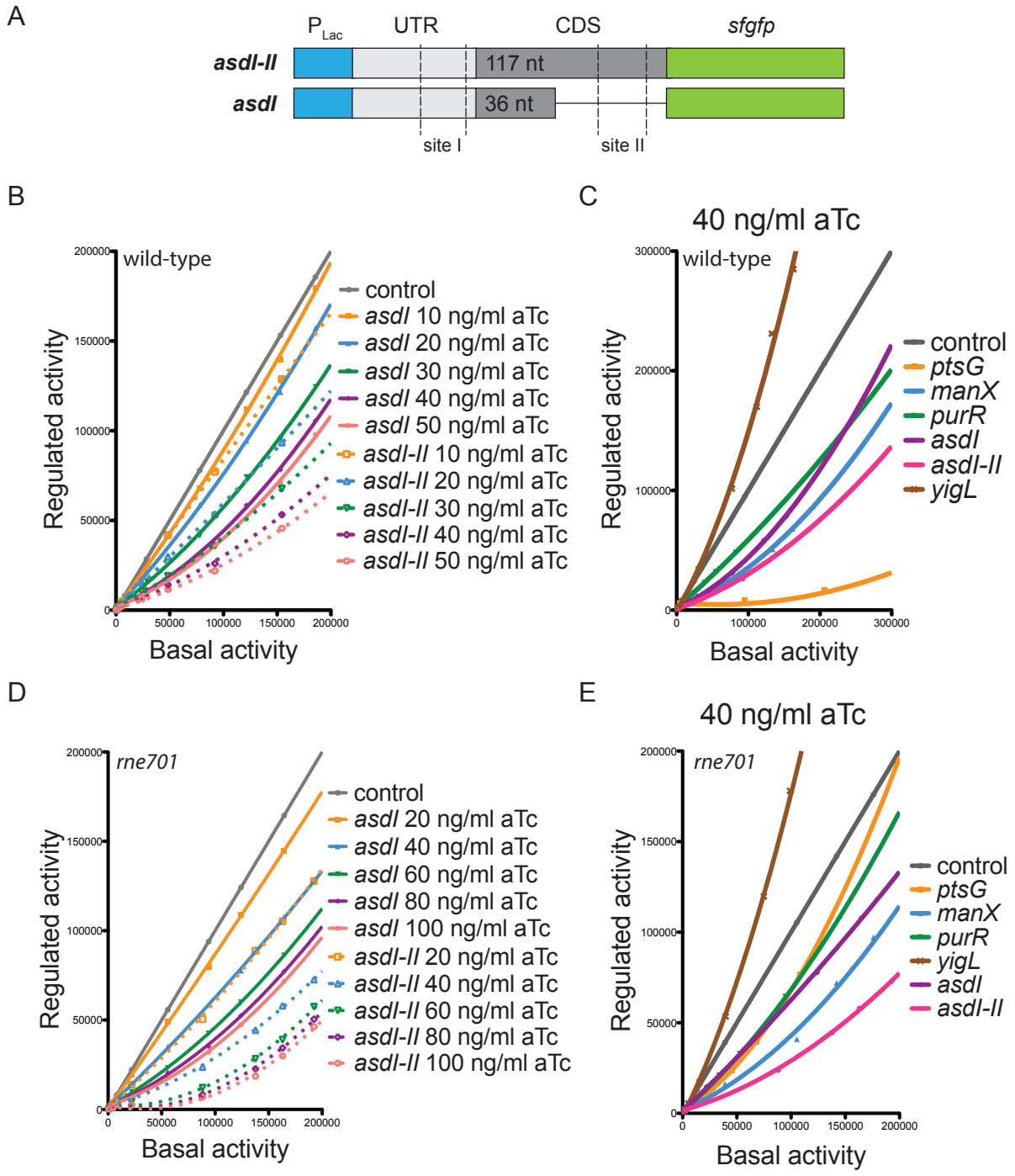

Figure 7. SgrS binding cooperativity allows for improved repression of *asd* translation. A) Illustration of *asdI* and *asdI-II* constructs with SgrS binding sites marked. Graphs show comparison of SgrS regulation of *asdI* and *asdI-II* variants in (B) wild-type and (D) *rne701* mutant by plotting regulated activity over basal activity at various SgrS expression levels (20-100 ng/ml aTc). Regulatory hierarchy of SgrS targets in (C) wild-type and (E) *rne701* mutant strains. Regulation of target genes at one SgrS expression level (40 ng/ml aTc) are compared by plotting regulated activity over basal activity of the *gfp* reporter.

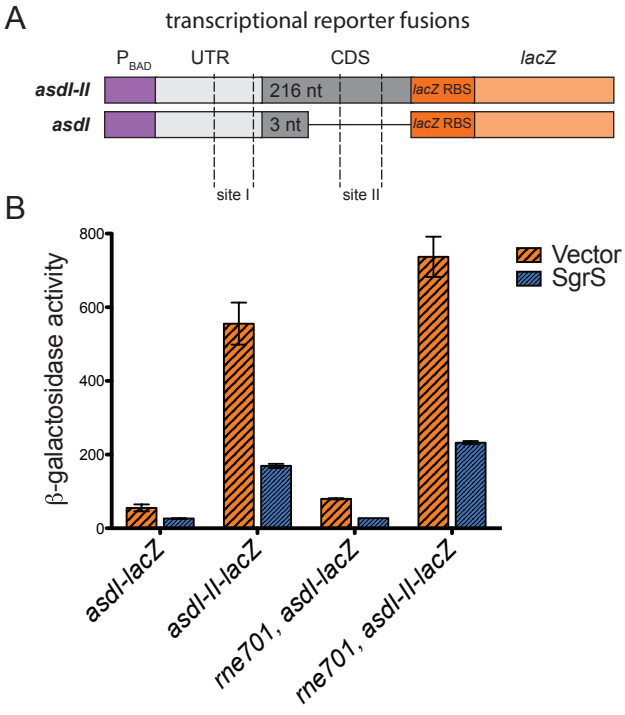

Figure 8. SgrS regulation of transcriptional *asd-lacZ* fusions. β-galactosidase activity of (A) *asdI-lacZ* (+1 to +64) and *asdI-II-lacZ* (+1 to +277) was (B) assayed in response to SgrS expression from a plasmid (and vector control) in WT and *rne701* background strains.